

# MEMS fabrication based on nickel-nanocomposite: film deposition and characterization

Kwok-Siong Teh<sup>1</sup>, Yu-Ting Cheng<sup>2</sup> and Liwei Lin<sup>1</sup>

<sup>1</sup> Berkeley Sensors and Actuators Center & Department of Mechanical Engineering, University of California, 497 Cory Hall, Berkeley, CA, USA

<sup>2</sup> Department of Electronics Engineering, National Chiao Tung University, Hsinchu, Taiwan, Republic of China

E-mail: [kwok.siong@gmail.com](mailto:kwok.siong@gmail.com)

Received 3 April 2005, in final form 26 September 2005

Published 26 October 2005

Online at [stacks.iop.org/JMM/15/2205](http://stacks.iop.org/JMM/15/2205)

## Abstract

Electrosynthesized metal-nanocomposites represent a unique class of microelectromechanical systems (MEMS) structural material due to their compatibility with MEMS and CMOS fabrication technologies via a one-step, selective on-chip deposition process at low temperatures ( $\sim 50\text{--}90^\circ\text{C}$ ). In this paper, particle-reinforced, electrosynthesized nickel-nanocomposites of various compositions have been successfully demonstrated as potential structural materials for MEMS. We have achieved low-temperature, stress-free, wafer-level fabrication of nano-composite MEMS via both an electroless nickel (EN) and an electrolytic nickel (EL) deposition process, with the addition of uniformly dispersed micro- and nanoparticles of either cordierite (diameter  $\approx 100\text{ nm--}5\ \mu\text{m}$ ) or diamond (diameter  $\sim 4\text{ nm}$ ). The as-deposited nickel-cordierite films exhibit better thermal compatibility with silicon, compared to nickel. The measured coefficients of thermal expansion (CTE) of EN-cordierite and EN are  $17.34\text{ ppm K}^{-1}$  and  $26.69\text{ ppm K}^{-1}$ , respectively. Stress-temperature measurement of EN-cordierite composite also confirms that residual stress decreases with the incorporation of cordierite. Finally, by adding various concentrations of nanodiamond particles into an EL matrix, it is found that higher diamond concentration renders these films more compressively stressed.

(Some figures in this article are in colour only in the electronic version)

## 1. Introduction

Since its birth, the development of microelectromechanical systems (MEMS) has been accelerated tremendously by leveraging mature manufacturing technologies from the semiconductor industry. This is especially remarkable from a material standpoint, where silicon (Si) has been utilized extensively and almost exclusively as the structural material for planar, movable MEMS structures such as the microresonator [1], microgyroscope [2], micromirror [3] and radio frequency (RF) microrelay [4]. As a structural material, Si is extremely robust and versatile, which is attributed to the rich

repertoire of fabrication methods, and its excellent mechanical properties such as high Young's modulus ( $\sim 160\text{ GPa}$ ), yield strength ( $\sim 7\text{ GPa}$ ) and respectable fatigue strength [5]. However, challenges and opportunities exist to further explore promising materials and fabrication technologies in order to extend the operation ranges and applications of MEMS devices.

One of the fundamental requirements of a silicon deposition process lies in its inherent high processing temperature—as above-average quality polysilicon films are generally produced around  $600^\circ\text{C}$ . Although research has been done on low temperature polysilicon films, the results were less

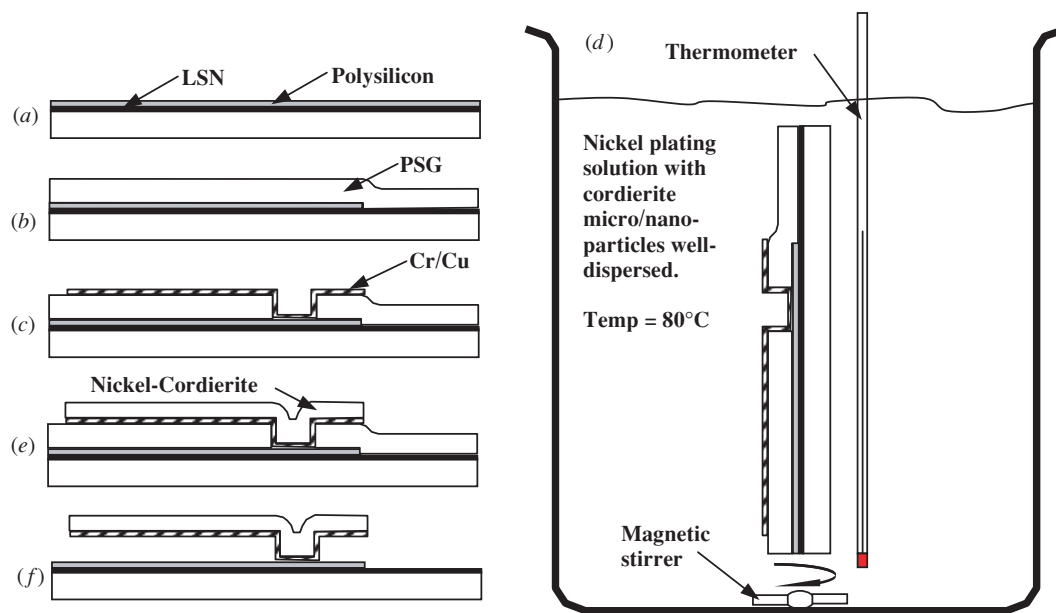


**Figure 1.** The three-mask fabrication process begins with (a) the deposition of 4000 Å of low stress silicon nitride (LSN) and 5000 Å of phosphorous-doped polysilicon on top of a Si wafer. (b) Polysilicon is then reactive-ion etched by chlorine gas ( $\text{Cl}_2$ ) to define the ground plane and interconnects. A  $2\ \mu\text{m}$  thick sacrificial LPCVD phosphosilicate glass (PSG) is next deposited. This is followed by (c) patterning the PSG for the anchor area, and patterning sputtered Cr/Cu ( $150\ \text{Å}/600\ \text{Å}$ ) with a lift-off process. (d) The processed wafer is then seeded in Pd solution, immersed in a nickel-composite plating solution to selectively grow a nickel-composite thin film. During the film growth process,  $\text{Ni}^{2+}$  ions are reduced by the hypophosphite ions to produce the nickel film, which embeds nanoparticles simultaneously, yielding the structure in (e). Hydrogen gas is also evolved during this process. (f) 49% HF solution is used to release the structure by etching away the sacrificial PSG layer prior to a supercritical  $\text{CO}_2$  release.

than ideal [6]<sup>3</sup>. Therefore, the thermal budget requirement prohibits the direct post-CMOS deposition and processing of polysilicon micro structures. From the technology perspective, assembling silicon-based microstructures onto microelectronics in a post-CMOS manner not only demands highly precise spatial alignment, but also invariably introduces other challenges such as bonding of parts, interfacial integrity during the integration process, residual stress and possible damage to the components during the post-CMOS processes.

Such a dilemma has rekindled *de novo* the research on alternative MEMS structural materials with low processing temperatures and good CMOS-compatibility. In the area of polysilicon-based surface-micromachining processes, polysilicon-germanium, or PolySiGe, remains the front-runner in this aspect, as it can be deposited at a temperature that is almost CMOS compatible [7, 8]. On the other hand, metals, being good conductors, and capable of being processed via a large collection of processing technologies at low cost, would also be good candidates as MEMS structural materials. Metal-based microstructures had been studied before the emergence of polysilicon, yet they suffered from mechanical deficiencies such as aging and fatigue [9]. To overcome these challenges, previous studies have shown that the inclusion of second-phase micro- and nanoparticles in a ductile metal matrix could improve the mechanical strength and thermal properties through a composite effect [10, 11]. Two mechanisms contribute to this composite effect: (1) load-transfer from low-strength, ductile matrix to high-strength, high-stiffness

particles (for  $\mu\text{m}$  particles), and (2) strain-hardening due to resistance to dislocation movement via dislocation pinning (for smaller, nm-sized particles). Hence, an optimal solution would be the addition of micro- and nanoparticles into metal MEMS structures to potentially strengthen the material properties, with the added advantage of low temperature processing and feasibility for direct integration with microelectronics. We have previously discovered that the incorporation of cordierite nanoparticles in a blanket nickel film is capable of attenuating the effect of thermal mismatch between a silicon substrate and an EN film. This is achieved without compromising Young's modulus and electrical conductivity of the EN film [12, 13]. This preliminary evidence also provides a plausible premise for us to hypothesize that one may indeed increase the stiffness of the nickel film by embedding extremely hard and stiff nanoparticles, such as nanodiamond, in the metal matrix. In this paper, we will demonstrate the fabrication of microstructures via this technology, with preliminary results on material characterization.

## 2. Design and fabrication

Figure 1 illustrates the fabrication of nickel-nanocomposite suspended microstructures on a standard semiconductor platform built on polysilicon and silicon nitride ( $\text{Si}_x\text{N}_y$ ) layers, via a three-mask surface micromachining process. The process begins with the blanket deposition of a layer of a low pressure chemical vapor deposited (LPCVD) silicon nitride film (4000 Å) that serves as an insulation layer. Next, a conductive, phosphorous-doped polysilicon layer (5000 Å) is deposited via LPCVD, and subsequently patterned using

<sup>3</sup> Philips Research, part of Koninklijke Philips Electronics N.V., [www.research.philips.com](http://www.research.philips.com).

the photolithographic method to define the ground layer and electrical interconnects. The anchor region of the microstructure is next defined on a layer of sacrificial phosphosilicate glass (PSG) and  $\text{CF}_4$  plasma etched. Besides acting as a sacrificial layer, the phosphorous-rich PSG also serves as an *in situ* n-doping source (phosphorous) for the underlying polySi during the subsequent annealing/drive-in step in  $\text{N}_2$  environment, which helps reduce the sheet resistance of the polySi further.

For EN Ni or EN Ni-nanocomposite plating, a thin primary seed layer (150 Å/600 Å) is next sputtered and lifted off to define the plating region. Using copper (Cu) as the top catalytic surface, subsequent activation in palladium (II) chloride ( $\text{PdCl}_2$ ) solution ensues, before the wafers are plated in pure EN Ni or second phase containing colloidal EN Ni bath. During the activation process, Pd forms a catalytic layer on the Cu surface, which acts as 'seed' or nucleation sites for EN Ni or EN Ni-composite to deposit. On the other hand, for EL Ni or EL Ni-nanocomposite plating, there is no strict restriction on the type of metal to be used as a conductive layer, as long as the metal does not oxidize easily in air or in aqueous solution, and is not reactive toward the plating solution. In this work, Cr/Cu or Cr/Au (150 Å/200 Å) is blanket-sputtered after patterning the PSG. This is then followed by a photolithographic step to define the photoresist mold, whereby EL Ni or EL Ni-nanocomposite selectively deposits later. Prior to the plating process, dry nanoparticles are dispersed in the plating bath by both mechanical stirring and sonication (30 min). While we have not investigated the chemistry for particulate dispersion, which is a major research undertaking in its own right, mechanical and ultrasonic perturbations have performed adequately in this preliminary study in creating a stable colloidal suspension that results in reasonable particle dispersion uniformity. The wafer is subsequently placed in a vertical fashion in the plating solution, which continued to be stirred at 120 rpm (EN Ni) and 250 rpm (EL Ni). The bath temperatures are maintained at 80 °C (EN) and 50 °C (EL) for optimum mechanical performance. A stable colloidal bath is especially crucial for EN Ni-nanocomposite plating. It is, therefore, of critical importance to ensure that the second phase chosen is not catalytic toward  $\text{Ni}^{2+}$  reduction; else catastrophic precipitation may occur where metals rapidly precipitate out of the solution in an uncontrollable manner. In addition, particulate contaminants (with catalytic properties) should be thoroughly removed by filtering before heating the solution to the target plating temperature to avoid undesirable metal precipitation.

During the plating process,  $\text{Ni}^{2+}$  ions in the solution continue to be reduced at the cathode or at the wafer, by acquiring cathodic electrons in the case of EL Ni, and via electron transfer from hypophosphate anions in the case of EN Ni. The reduced  $\text{Ni}^0$  formed metallic islands on the substrate surface, which gradually coalesce and morph into a continuous nickel film on the cathode. Another concurrently occurring event is the arrival of the micro- and nanoparticles in the vicinity of the plated surface brought about by convective current from mechanical agitation. Based on [14], upon immersion in a plating solution, the particles instantaneously acquire a sheath of surface charges by adsorbing ionic species ( $\text{Ni}^{2+}$ ). Together with the ions, these particles are transported

by convective current to the plating surface in a stochastic fashion, where their velocities become rapidly retarded by the existence of a hydrodynamic boundary layer. The particles then diffuse through the boundary layer toward the substrate surface. Upon close contact, some of the  $\text{Ni}^{2+}$  ions previously adsorbed on the particle surface are reduced and cause irreversible encapsulation of the particles in a growing Ni matrix.

### 3. Characterization and discussions

In this section, characterization work and discussions will be focused on several nanocomposite thin films, namely, EN Ni-cordierite, EN-Ni-diamond, EL Ni-diamond and EN-Ni-iron (II,III) oxide. Through material characterization, the objective of using different second phase nanoparticle systems is elucidated.

#### 3.1. Nickel-cordierite

Cordierite ( $2\text{MgO}\cdot 2\text{Al}_2\text{O}_3\cdot 5\text{SiO}_2$ ) is a fused particle containing oxides of Mg, Al and Si, with chemical composition (weight%) of  $\text{MgO} = 13.8$ ,  $\text{Al}_2\text{O}_3 = 34.8$  and  $\text{SiO}_2 = 51.4$ .<sup>4</sup> It has excellent thermal shock property and is used for a wide variety of high temperature applications. Moreover, its low dielectric loss property also lends itself to applications in electronics. With a coefficient of thermal expansion (CTE) of  $2.1 \text{ ppm K}^{-1}$ , the goal of using cordierite is to improve the CTE compatibility and to reduce CTE-induced thermal residual stress existing between EN Ni and Si, such that EN Ni can be engineered for use as MEMS structural material built on a Si-based substrate. We have previously discovered that the incorporation of cordierite nanoparticles in a blanket nickel film is capable of attenuating the effect of thermal mismatch between the silicon substrate and the EN film [12]. This is achieved without compromising Young's modulus and electrical conductivity of the EN film [13], as shown later in figures 5(a) and (b).

*3.1.1. Surface morphology and surface property.* Figures 2(a)–(d) show the scanning electron micrograph (SEM) and electron dispersive spectrum (EDS) of a 5  $\mu\text{m}$  thick EN-cordierite film after 30 min of deposition, respectively. Figure 2(a) illustrates the surface morphology of the nanocomposite film. The cross-sectional SEMs shown in figures 2(b) and (c) illustrate that there is a range of particles of various dimensions being embedded in the EN Ni matrix. From these SEMs, there are no visible interfacial material defects (cracks, delaminations), indicating the intimate bonding between the particles and the matrix. The SEMs show the extent of large spherical cordierite particles of 4–5  $\mu\text{m}$ , and smaller, submicron nanoparticles, being embedded in the EN Ni matrix. Figure 2(d) exhibits the EDS of an embedded nanoparticle. Figure 3 further shows that, while not optically visible, the existence of smaller, sub-micron nanoparticles within the EN Ni matrix can be confirmed by the EDS, as evident from the elemental peaks of Al, Mg, Si and O in figures 3(b)–(d), which are the constituent elements of the cordierite particles (Mg, Al, Si

<sup>4</sup> CeramTec North America Inc., One Technology Place, PO Box 89, Laurens, SC 29360-0089 (www.ceramtec.com).

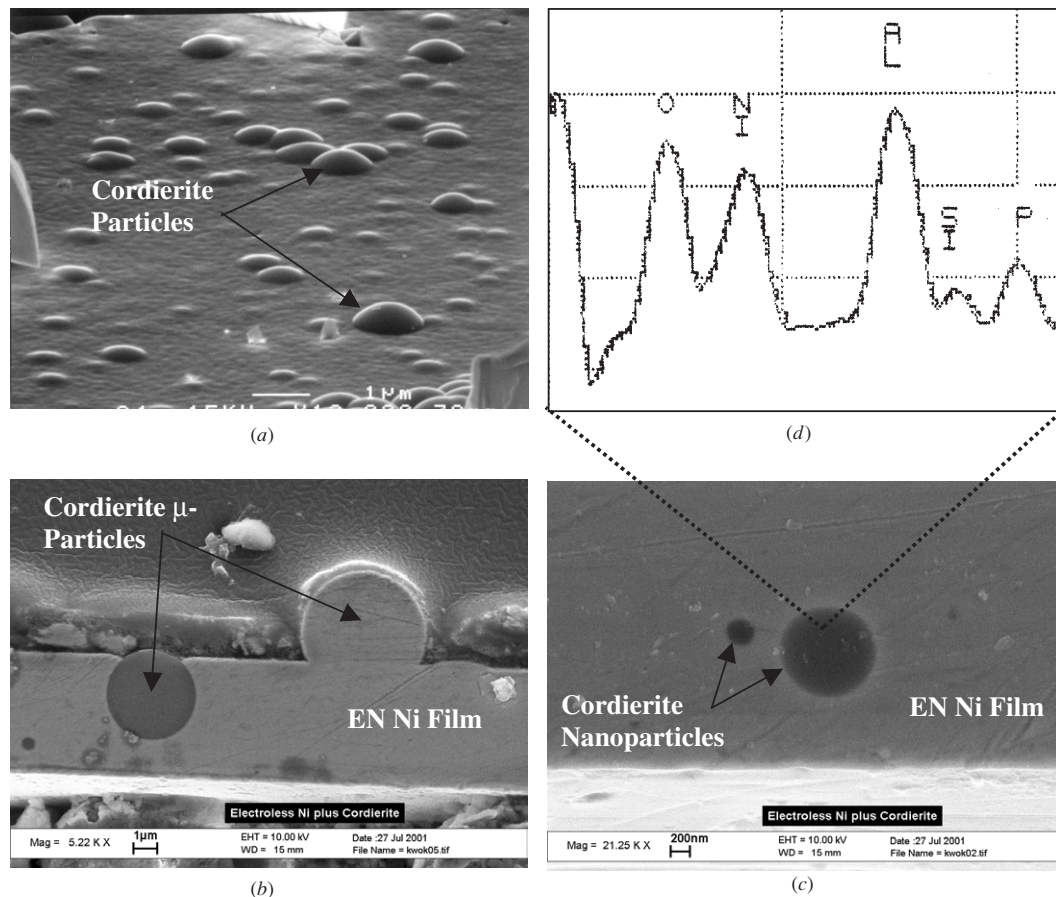


**Figure 2.** (Counter-clockwise from top-left) (a) An oblique view of a blanket-deposited electroless-nickel (EN Ni)-cordierite film shows that particles are well-embedded in the nickel matrix. (b) The cross-sectional view of a 5  $\mu\text{m}$  electroless-nickel-cordierite thin film grown on a Si/TaN/Ta/Cu substrate, showing the spherical cordierite particles. The cross-sectional SEM also reveals (c) cordierite nanoparticles. (d) EDS confirms the existence of sub-micron cordierite particles embedded within the electroless-nickel matrix. It also indirectly implies that particles of various sizes are well distributed within the matrix.

and O). These figures also show that the amount of phosphorus (P), indicating the reduction of hypophosphite ions to  $\text{P}^0$  during EN Ni plating, decreases as the thickness increases. This corresponds to the depletion of reducing agents ( $\text{HPO}_2^{2-}$ ) as plating proceeds.

**3.1.2. Fabricated device.** Figure 4 shows the suspended portion of a fabricated and released microstructure. The EDSs shown in figures 4(a) and (b) represent the surface elemental composition of the plated structure. Probing at two seemingly identical spots on the microresonator comb fingers, the EDSs reveal their compositional difference, and disclose the encapsulated cordierite nanoparticles. This shows that nanoscale cordierite particles could be encapsulated in the thin microresonator finger. Larger encapsulated particles may cause uneven nucleation of metal films and hence the film thickness; however, we believe this can be ameliorated by restricting particle sizes to be smaller than one-tenth of the characteristic dimension of the structure.

**3.1.3. Mechanical property—Young's modulus and hardness.** Figure 5(a) compares Young's modulus of 2  $\mu\text{m}$  thick EN Ni and EN Ni-cordierite films in their pre- and post-annealed states. Young's modulus is measured by means of a

nanoindentation test using a Nano Indentor<sup>®</sup> XP from MTS Systems Corporation. Cordierite has a slightly lower Young's modulus ( $\sim 128$  GPa (see footnote 4)) relative to electroless nickel ( $\sim 174$  GPa, as measured). It can be expected that the composite material will have a slightly lower Young's modulus, based on the rules of mixture. The volume fraction of the cordierite present in the thin film is estimated to be in the range 11–14% at a Young's modulus of 167 GPa. Since the density of cordierite ( $2600 \text{ kg m}^{-3}$ ) is smaller than that of nickel ( $8070 \text{ kg m}^{-3}$ ), the effective ratio of Young's modulus to the density of the composite film, in fact, can be increased by up to 5% in comparison with pure silicon. By varying the amount of particles present inside the film, the film property will be changed accordingly. Further investigation on the relationship between the particle concentration and film properties will be necessary.

Figure 5(b) illustrates the effect of cordierite particles on the hardness of the thin film. As shown, prior to annealing, the Berkovich hardnesses of both nickel and nickel-cordierite seemingly have no huge difference. However, when annealing at 400  $^\circ\text{C}$  is carried out, the hardness of nickel increases to 11.6 GPa whereas that of nickel-cordierite rises to 9.8 GPa. The increase in hardness is due to the precipitation of an intermetallic phase  $\text{Ni}_3\text{P}$ , and the increase in grain

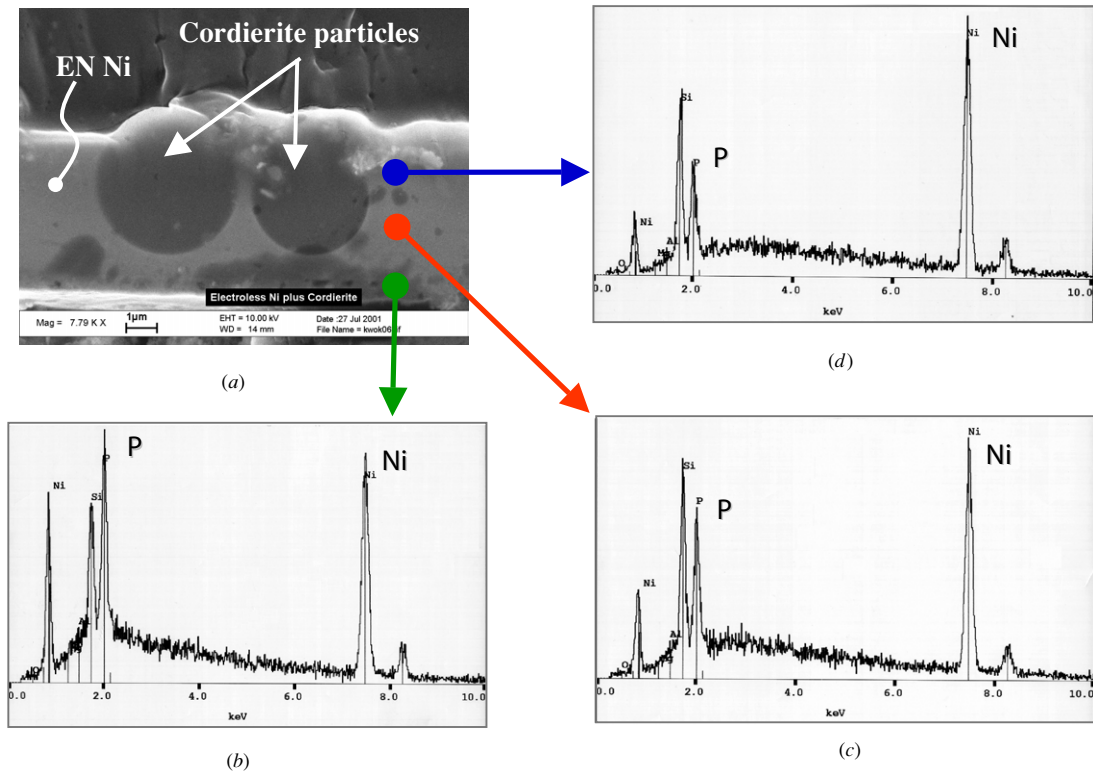


**Figure 3.** (Counter-clockwise from top left) (a) The cross-sectional SEM of an electroless-nickel (EN Ni)-cordierite film. (b)–(d) The elemental composition of the film from nearest to the substrate (b) to the top surface (d). As seen, the decrease in the amount of P corresponds to the depletion of reducing agents as plating proceeds over time.

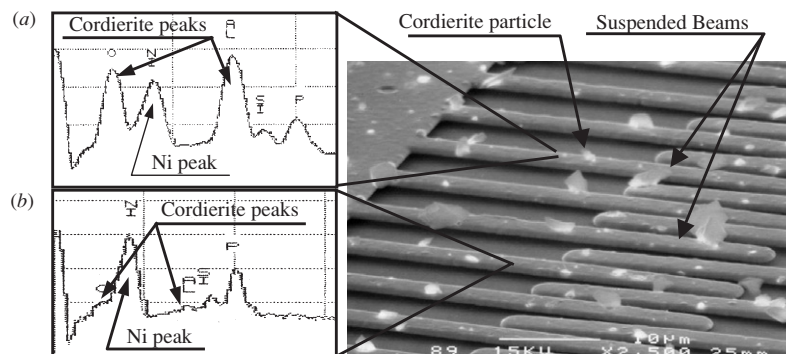


**Figure 4.** The SEM of a released, stress-free electroless-nickel (EN Ni)-cordierite microcantilever beam array. The two energy dispersive spectroscopy (EDS) graphs show the elemental composition of the top surface of the electroless-nickel (EN-Ni)-cordierite suspended beam. (a) The electron beam focusing on the visible particle shows that cordierite is the dominant species, but encapsulated in a thin layer of a nickel film (indicated by the presence of the Ni peak). (b) The electron beam focusing on a general area with no visible cordierite particles shows the weak signals of cordierite, and provides evidence that nanoscale particles could be scattered within the electroless-nickel matrix. The width of a plated microcantilever beam is  $\sim 3.75 \mu\text{m}$ , inter-beam spacing is  $\sim 0.5 \mu\text{m}$  and beam thickness is  $\sim 1 \mu\text{m}$ .

size [15]. The precipitation hardening effect might be due to the possibly denser spatial arrangement of the fine  $\text{Ni}_3\text{P}$  phase which increases the hardness of the electroless nickel film to a greater extent than cordierite is capable of.

**3.1.4. Coefficient of thermal expansion (CTE).** The CTE reduction of the EN Ni film through cordierite incorporation is evident from the CTE measurements carried out using a Flexus FLX-2320<sup>TM</sup> Laser-Interferometer in a temperature-controlled environment. The interferometer measures the

curvatures of as-deposited (on p-Si substrates) blanket films of EN Ni and EN Ni-cordierite as the temperature is gradually raised from ambient temperature to  $150^\circ\text{C}$  at approximately  $0.5^\circ\text{C min}^{-1}$ , and then cycled back to ambient temperature. Based on the curvatures of the film at specific temperatures, which in our experiments refer to the room temperature ( $25^\circ\text{C}$ ) and the deposition temperature ( $80^\circ\text{C}$ ), film stress is calculated by means of a biaxial thin film equation as follows:

$$\sigma(T) = \left( \frac{E}{(1-\nu)} \right) \left( \frac{h^2}{6Rt} \right) \quad (1)$$

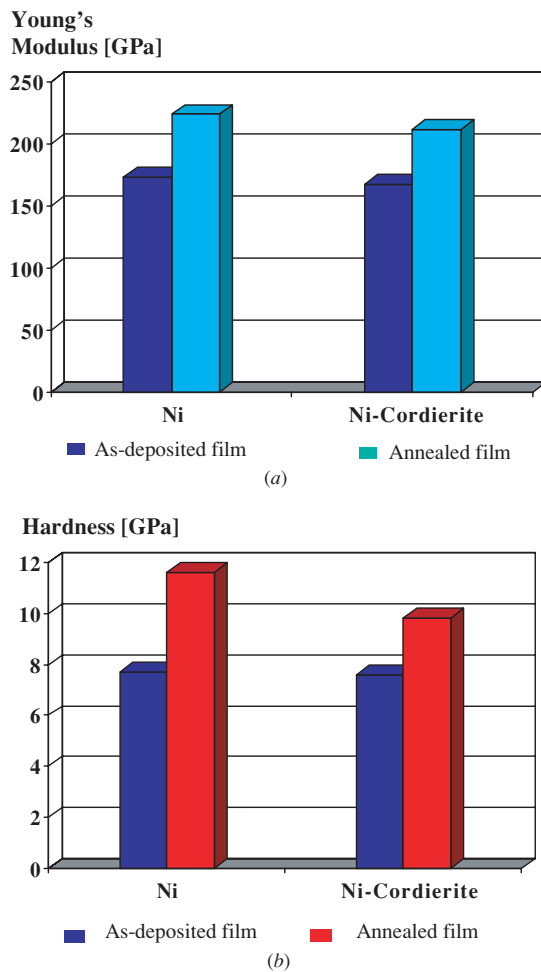


**Figure 5.** (a) Comparison of Young's moduli of pure electroless-nickel (EN Ni) and electroless-nickel (EN Ni)-cordierite films in their pre- and post-annealed states. (b) Comparison of the Berkovich hardnesses of electroless-nickel and electroless-nickel-cordierite films in their pre- and post-annealed states.

where  $\sigma(T)$  is the temperature-dependent film stress (Pa),  $(E/(1-\nu))$  is the biaxial elastic modulus of the substrate ( $1.805 \times 10^{11}$  Pa for p-Si(100)) (Pa),  $h$  is the substrate thickness ( $525 \mu\text{m}$  in this case) (m),  $R$  is the radius of curvature of the substrate (m) and  $t$  is the thin film thickness (m).

The CTE of the composite thin film,  $\alpha$ , is next calculated based on the thermal stress equation,

$$\sigma(T) = \left( \frac{E}{(1-\nu)} \right) \cdot \alpha \cdot \Delta T. \quad (2)$$

Figures 6(a) and (b) portray the post-annealed states of EN Ni and EN Ni-cordierite films. While EN Ni suffers from substantial delamination due to thermal mismatch, the EN Ni-cordierite film shows better thermal compatibility with silicon substrates. Figure 6(c) exhibits the as-measured CTEs of both EN and EN-cordierite films, *vis-à-vis* polysilicon and cordierite. The as-measured CTE of EN is  $26.69 \text{ ppm K}^{-1}$ , yet it reduces to  $17.34 \text{ ppm K}^{-1}$  for the EN-cordierite film (CTE of cordierite being  $2.1 \text{ ppm K}^{-1}$  (see footnote 4)). This shows a marked improvement in terms of stress compatibility between

the EN Ni-cordierite film and the underlying Si substrate. From the rules of the mixture equation,

$$\alpha = \alpha_m + (\alpha_p - \alpha_m)V_p \quad (3)$$

where  $\alpha$ ,  $\alpha_m$  and  $\alpha_p$  are the CTEs of the composite, matrix and particle, respectively; and  $V_p$  is the volume fraction (v/v) of the particle—an approximated 38% v/v of cordierite occupies the EN matrix. By increasing the volume fraction of cordierite further, the CTE is expected to lower proportionally.

**3.1.5. Thermal residual stress.** The thermal residual stress is measured by means of a Flexus FLX-2320<sup>TM</sup> Laser-Interferometer, in a similar fashion as described in section 3.1.4. As shown in figure 7(a), the as-measured thermal residual stress reverses (from tensile to compressive, with respect to p-Si) as the film temperature is gradually raised from  $30 \text{ }^\circ\text{C}$  to  $150 \text{ }^\circ\text{C}$ . The point of zero stress coincides with the plating temperature, that is, approximately  $80 \text{ }^\circ\text{C}$ . Although both EN Ni and EN Ni-cordierite films stress-relieve with increasing temperature, cordierite ameliorates not only the thermal residual stress of the EN Ni film to begin with ( $34.2 \text{ MPa } \mu\text{m}^{-1}$  versus  $54.2 \text{ MPa } \mu\text{m}^{-1}$  for EN Ni at  $30 \text{ }^\circ\text{C}$ ), but nearly halves the temperature-dependent stress sensitivity ( $-0.525 \text{ MPa } \mu\text{m}^{-1} \text{ K}^{-1}$  versus  $-0.937 \text{ MPa } \mu\text{m}^{-1} \text{ K}^{-1}$  for EN Ni), as evident from the smaller stress-temperature gradient. This indicates that EN Ni-cordierite nanocomposite could be used as a structural material for MEMS that requires structural and mechanical integrity at elevated temperature.

Figures 7(a) and (b) juxtapose fabricated EN Ni and EN Ni-cordierite microresonators alongside each other. Figure 7(a) shows a partially released EN Ni microresonator deforming out-of-plane due to a thermal residual stress gradient formed during post-deposition cooling. The EN-cordierite microresonator in figure 7(b) is plated in a plating bath that contains  $4 \text{ g l}^{-1}$  of well-dispersed cordierite micro- and nano-particles. As shown in figure 7(b), no out-of-plane deformation is observed for a fully released EN Ni-cordierite microresonator. This qualitatively demonstrates that the addition of an adequate volume fraction of cordierite particles in the EN matrix is capable of evening out the stress gradient between Si and EN Ni by reducing the CTE difference between them, and hence substantially negating the effect of thermally induced residual stress. While the overarching goal has been to fabricate a microresonator that is capable of achieving high resonating frequency, due to possible electrical shorting resulting from the protruding granular structures between the resonator comb fingers, the authors believe that further effort in eliminating electrical shorting is necessary before successful actuation is possible.

**3.1.6. Electrical resistivity.** Since MEMS microstructures are to be actuated electrically, electrical resistivity change due to cordierite incorporation is examined. Figure 8 compares the resistivity of the EN Ni and EN Ni-cordierite films in their pre-annealed and post-annealed states. It is shown that the incorporation of cordierite particles does not compromise the resistivity of the composite material. Hence, it might be inferred that, below a certain threshold concentration

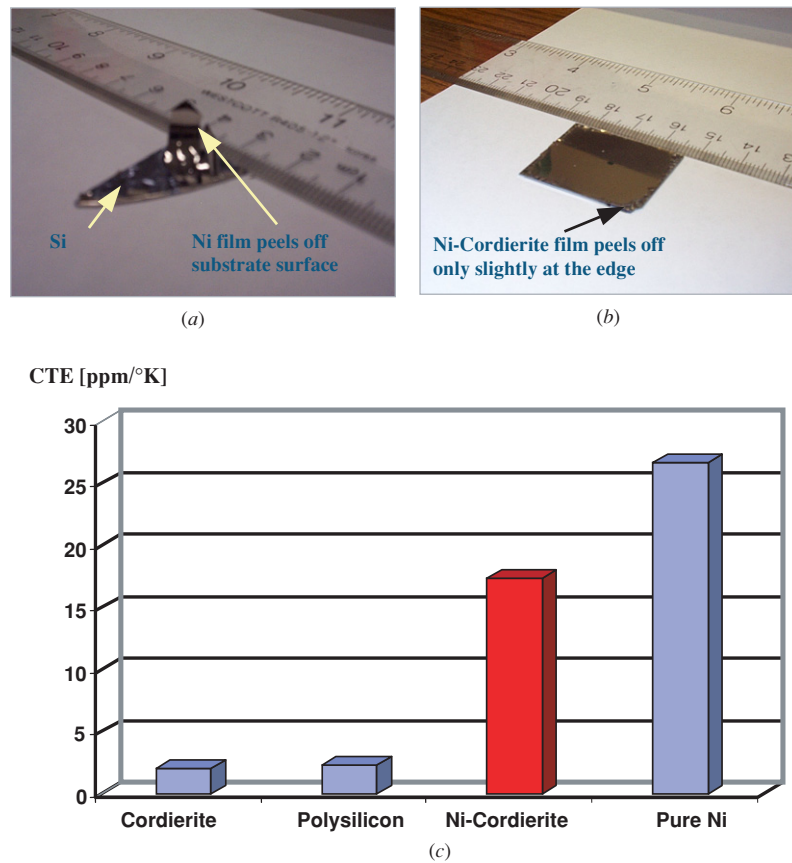


**Figure 6.** Electroless-nickel and electroless-nickel-cordierite films were subjected to  $N_2$  annealing at  $400\text{ }^\circ\text{C}$  for 2 h. (a) The electroless-nickel film peels off the substrate surface due to thermal mismatch. (b) Electroless-nickel-cordierite films are relatively intact, demonstrating thermal compatibility with substrate. (c) Comparison of the CTE of cordierite, polysilicon, electroless-nickel-cordierite and electroless-nickel. Electroless-nickel has an as-measured CTE of  $26.7\text{ ppm K}^{-1}$ , while cordierite has a CTE of  $2.1\text{ ppm K}^{-1}$ . By embedding cordierite particles in the pure nickel matrix, the effective CTE of electroless-nickel-cordierite is reduced to  $17.34\text{ ppm K}^{-1}$ . The CTE of polysilicon is  $2.33\text{ ppm K}^{-1}$ .

(‘percolation threshold’), cordierite particles have negligible effects on the resistivity of the composite thin film, which bodes well for electrical actuation of MEMS microstructures.

### 3.2. Nickel-nanodiamond

The preliminary evidence from EN Ni-cordierite provides a plausible premise for us to hypothesize that, due to the extreme hardness ( $\sim 90\text{ GPa}$ ), stiffness ( $1050\text{ GPa}$ ) and temperature resistance of diamond particles [16, 17], the incorporation of nanodiamond particles may enhance the overall stiffness of the nickel film, as well as its temperature resistance. A nanocomposite with such mechanical characteristics will have potential applications for devices that operate in the high frequency regimes, such as RF metal contact or relay switches and scanning micromirrors. To this end, we have fabricated microbeams of  $50$  (length)  $\times$   $2$  (width)  $\times$   $1$  (thickness)  $\mu\text{m}^3$ , and microcantilever beams as shown in figures 9(a) and (b), respectively.

**3.2.1. Fabricated device.** Figure 9(a) shows the oblique view of an SEM of a microbeam array made with EN Ni-nanodiamond composite. Figure 9(b) shows the top view of a

microcantilever beam array made from EL-Ni nanodiamond. As shown in figure 9(b), the diamond clusters reflect lights incident from a horizontal direction under a dark field optical microscope. The inset in figure 9(b) shows the TEM of the diamond particles used to fabricate these structures, which are on average approximately  $4\text{ nm}$  in diameter (as received from Nanostructured & Amorphous Materials, Inc.).

**3.2.2. Thermal residual stress.** Figure 10 shows that the as-measured thermal residual stress decreases as the  $1\text{ }\mu\text{m}$  EN Ni and EN-Ni-nanodiamond film temperatures are gradually raised from  $40\text{ }^\circ\text{C}$  to  $200\text{ }^\circ\text{C}$ . Behaving in a similar fashion as EN Ni-cordierite, diamond nanoparticles reduce the thermal residual stress of the EN Ni film from  $-4.06\text{ MPa }\mu\text{m}^{-1}\text{ K}^{-1}$  to  $-1.87\text{ MPa }\mu\text{m}^{-1}\text{ K}^{-1}$ , as evident from the smaller stress-temperature gradient, and hence smaller sensitivity to temperature change. This evidence suggests that the temperature resistance of nickel can be improved by the addition of diamond. While it is outside the scope of this research paper to explore the suitability of EN Ni-nanodiamond as a high-temperature MEMS material, we believe it may be feasible through optimizing the nanodiamond concentration to the extent that it both minimizes the thermal

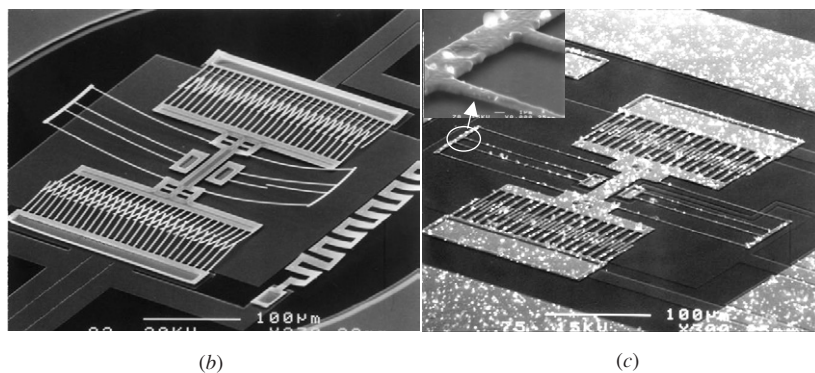


**Figure 7.** (a) When the film temperature is raised gradually from 30 °C to 150 °C, the as-measured nominal film stress (thermal residual stress (MPa) per unit thickness ( $\mu\text{m}$ )), of electroless-nickel (EN Ni) is reduced by uniformly incorporating cordierite particles. Electroless-nickel-cordierite undergoes less stress relaxation due to the nanocomposite effect, as shown by the smaller stress–temperature gradient. (b) A partially released, internally stressed electroless nickel microresonator. (c) A fully released, unannealed, residual stress free, electroless-nickel-cordierite microresonator. The addition of cordierite particles significantly reduces the residual stress. The inset shows a magnified view of the released double-folded beam.

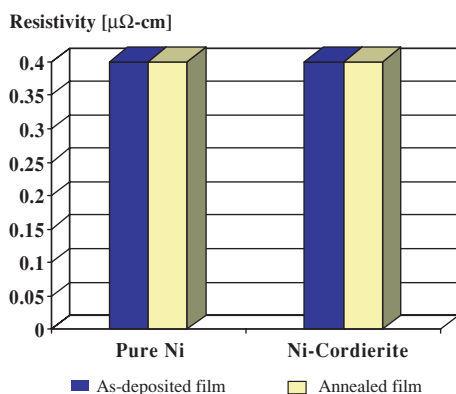


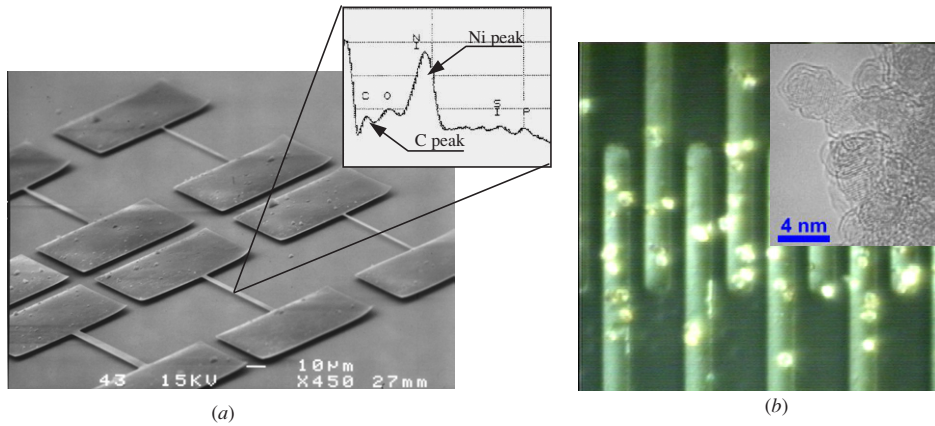
**Figure 8.** Comparison of the electrical resistivity values of electroless-nickel and electroless-nickel-cordierite films in their pre- and post-annealed states. The incorporation of ceramic particles into the nickel matrix clearly does not compromise the conductivity of the thin film.

residual stress and lowers the temperature sensitivity of the composite film.

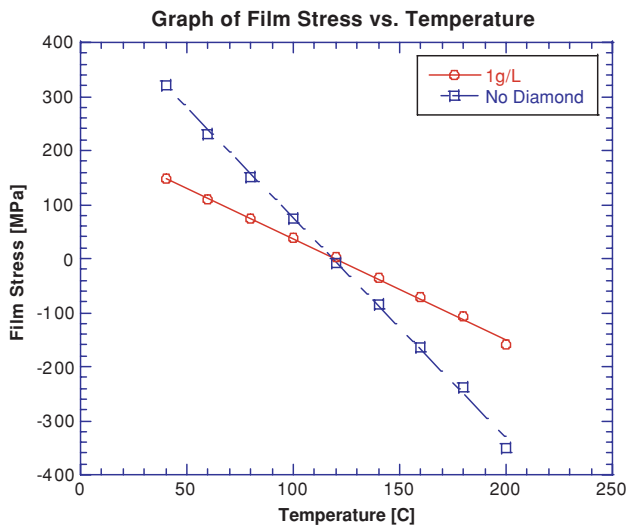
### 3.2.3. Thermal residual stress versus particle concentration.

Figure 11 shows the effect of the number of nanodiamond particles on the residual stress of an EL Ni thin film. EL Ni-nanodiamond films were blanket-deposited onto p-silicon, which were first seeded with Ti/Au. As shown in figure 11, as the amount of nanodiamond particles increases from  $0 \text{ g l}^{-1}$  to  $1 \text{ g l}^{-1}$  and  $3 \text{ g l}^{-1}$ , the stress state on an originally tensile-stressed EL Ni film becomes less tensile. From a thermal consideration, when the Ni film is cooled down from 50 °C to room temperature, it will undergo a larger contraction than p-Si due to the differential in CTE. On the other hand, with a much lower CTE at  $0.8 \times 10^{-6} \text{ ppm K}^{-1}$ , diamond does not contract as much (compared to  $12\text{--}17 \times 10^{-6} \text{ ppm K}^{-1}$  for nickel, and  $2.6 \times 10^{-6} \text{ ppm K}^{-1}$  for Si). The effect of nanodiamond inclusion resembles that of cordierite in terms of CTE reduction.

We also hypothesize that, due to the thermal mismatch between nanodiamond, nickel and silicon, each nanodiamond particle may induce a spatially strained nickel lattice around its perimeter, and hence precipitate a distorted, compressive stress field at its interface and in its vicinity. By examining the plated EL Ni-nanodiamond film, we found that no microcracks



**Figure 9.** (a) The electroless-nickel-nanodiamond microbeam array. The EDS shows that diamond nanoparticles are incorporated within the electroless-nickel matrix. (b) A dark field optical micrograph of the suspended microcantilever beams shows the embedment of sub-micron diamond particles. The inset is a TEM of the nanodiamond particles used in this fabrication (average diameter  $\sim 4$  nm).



**Figure 10.** The composite effect of diamond nanoparticles manifests itself via film stress reduction. When the temperature increases from  $40^{\circ}\text{C}$  to  $200^{\circ}\text{C}$ , electroless-nickel-nanodiamond shows less sensitivity to the temperature compared to the electroless-nickel film, as shown by the smaller gradient of the curve.

exist in the film. This leads us to assume that the interfacial strength between nickel and diamond is good, and could be higher than the yield strength of nickel. This may cause the relatively softer nickel in between the nanoparticles to be compressed and deformed elasto-plastically. In the case where the magnitude of such deformation is small, the plastic component may be ignored and upon final device release, the material will release the elastic strain energy by deforming out-of-plane, as shown in figure 7(b). The overall effect is thus dependent on the density of the strain fields, hence the concentration of diamond particles embedded within the Ni matrix, as illustrated by the decreasing trend in figure 11. It is also noted that the stress state of EL Ni (26.6 MPa) at room temperature is significantly lower than EN Ni (321 MPa). This is expected since EN Ni is deposited at higher temperature, and EN Ni typically

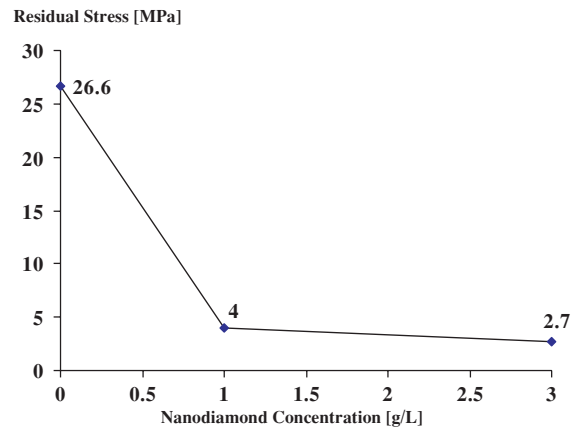


**Figure 11.** The effect of the addition of various concentrations (grams of nanodiamond per liter of plating solution) of nanodiamond into a nickel matrix is manifested in its residual stress values. The higher the concentration of nanodiamonds being incorporated into the matrix, the more compressive the stress state of the matrix becomes.

produces denser and harder films due to the presence of P.

### 3.3. Nickel-iron(II, III) oxide

In addition to the CTE, the ferromagnetic property of an electroless nickel film can also be enhanced by incorporating Fe(II, III) oxide powders. Figures 12(a) and (b) show the SEM of a  $2\ \mu\text{m}$  thick Ni-Fe(II, III) oxide composite film identified through EDS. The measurement of the magnetic moment versus magnetic field curves as illustrated in figure 12(c) shows the tremendous improvement of the coercivity of electroless nickel of up to 170 Oe by the addition of Fe(II, III) oxide. Based on this experimental measurement, it is evident that Fe(II, III) can be easily co-deposited onto a nickel film to modify its magnetic property and therefore could be useful in the fabrication of magnetic MEMS.

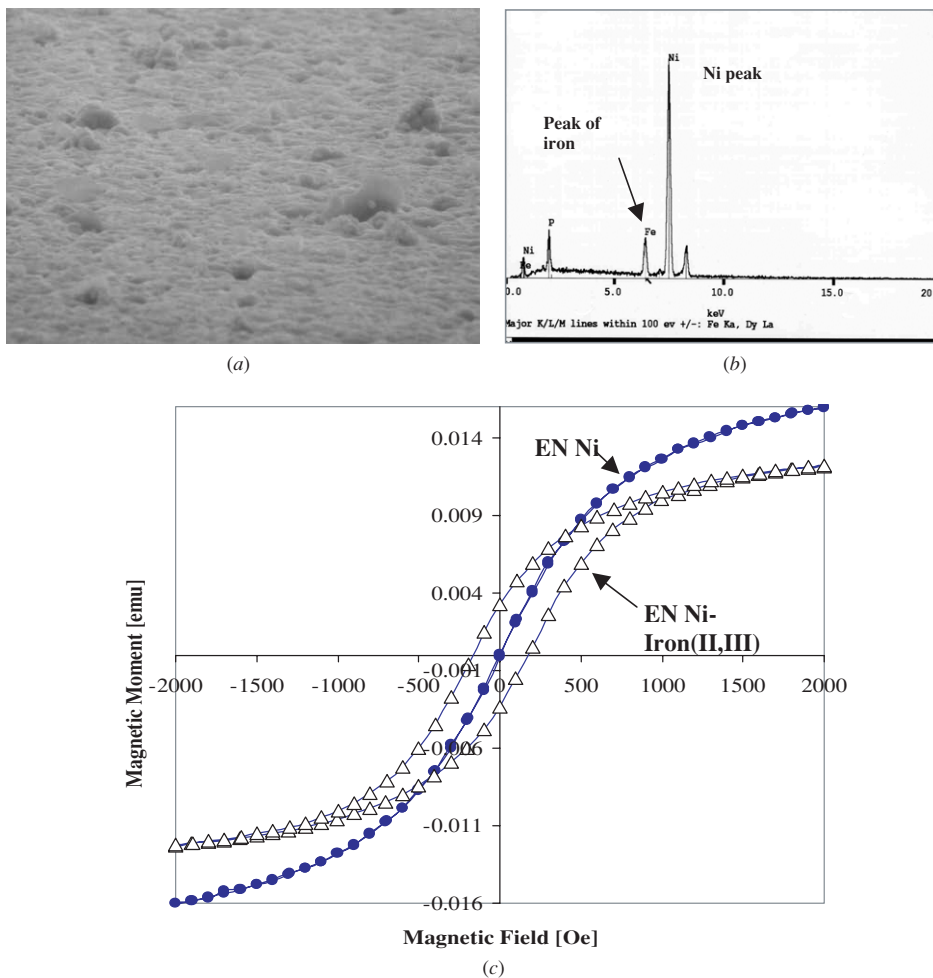


**Figure 12.** (a) The SEM of the as-deposited electroless-nickel (EN Ni)-iron(II, III) oxide film and (b) EDS showing the surface composition of the film and confirming the encapsulation of iron(II, III) oxide nanoparticles in electroless nickel. (c) Comparison of the ferromagnetic properties of electroless-nickel and electroless-nickel-iron (II, III) oxide composite films. The nickel film does not exhibit coercivity, while the electroless-nickel-iron (II, III) oxide film shows a coercivity of up to 170 Oe.

#### 4. Conclusions

EN and EL Ni-nanocomposites of various compounds have been demonstrated and their physical properties characterized and discussed. It is found that each nanoparticle has a distinct characteristic that lends itself for use under specific engineering requirements. EN Ni-cordierite has been found to be thermally compatible with Si substrate, and it helps ameliorate thermal residual stress incompatibility between Si and EN Ni. EN Ni-iron(II, III) oxide has been found to achieve a coercivity of 170 Oe, making EN Ni-iron(II, III) oxide plating a possible means to fabricate magnetic microstructures. Finally, the incorporation of extremely hard nanodiamond particles into EN Ni may be a viable solution for making high stiffness microstructures.

#### Acknowledgments

The authors would like to acknowledge the valuable inputs on electroless and electro-plating of Ni from Dr Carlos Sambucetti (formerly at IBM T J Watson Research Center) and Dr Li-Wei Pan (Perkins Elmer Optoelectronics). These devices were fabricated in the UC-Berkeley Microfabrication

Laboratory and this work has been supported in part under a grant from DARPA (F30602-00-2-0566). KST was supported in part by an Eastman Kodak Fellowship. YTC is supported in part by NSC 92-2215-E-009-043.

#### References

- [1] Tang W C, Nguyen T-C H and Howe R T 1989 Laterally driven polysilicon resonant microstructures *Proc. IEEE Workshop on Microelectromechanical Systems (Salt Lake City, UT, USA)* pp 53–9
- [2] Putty M W and Najafi K 1994 A micromachined vibrating ring gyroscope *Invited Paper, Technical Digest, Solid-State Sensors and Actuators Workshop (Hilton Head, SC, June)* pp 213–20
- [3] Su G D J 2001 MEMS high-quality micromirrors for optical interconnect and optical pick-up heads *PhD Thesis* UCLA, CA, USA
- [4] Yao J J 2000 RF MEMS from a device perspective *J. Micromech. Microeng.* **10** R9–38
- [5] Muhlstein C L, Brown S B and Ritchie R O 2001 High-cycle fatigue of single-crystal silicon thin films *J. Microelectromech. Syst.* **10** 594–600
- [6] Voutsas A T and Hatalis M K 1992 Structure of as-deposited low-pressure chemical vapor deposition silicon films at low

- deposition temperatures and pressures *J. Electrochem. Soc.* **139** 2659–65
- [7] Franke A E, Bilic D, Chang D T, Jones P T, King T-J, Howe R T and Johnson G C 1999 Post-CMOS integration of germanium microstructures *Proc. 12th Ann. Int. Conf. Micro Electro Mechanical Systems (Orlando, FL, USA)* pp 630–7
- [8] Sedky S, Fiorini P, de Moor P, Baert K and Vanhoof C 1999 Polycrystalline silicon germanium as a structural material for surface micromachining *Proc. 10th Int. Conf. Solid State Sensors and Actuators (Sendai, Japan)* pp 492–5
- [9] Nathanson H C and Wickstrom R A 1965 A resonant-gate silicon surface transistor with high-Q band-pass properties *Appl. Phys. Lett.* **7** 84–6
- [10] Warren R 1990 *Ceramic-Matrix Composites* (New York: Chapman and Hall)
- [11] Hull D 1981 *An Introduction to Composite Materials* (Cambridge: Cambridge University Press)
- [12] Teh K S, Cheng Y T and Lin L 2003 Nickel nanocomposite films for MEMS applications *12th Int. Conf. Solid State Sensors, Actuators and Microsystems (Boston, MA, 8–12 June)* pp 1534–7
- [13] Teh K S, Cheng Y T and Sambucetti C 2002 Selective plating of nickel composite films for MEMS applications *Proc. 15th Ann. Int. Conf. Micro Electro Mechanical Systems (Las Vegas, NV, USA)* pp 384–7
- [14] Celis J P, Roos J R and Buelens C 1987 A mathematical model for the electrolytic codeposition of particles with a metallic matrix *J. Electrochem. Soc.* **134** 1402
- [15] Lowenheim F A 1978 *Electroplating* (New York: McGraw-Hill) pp 389–409 chapter 17
- [16] Angus J C 1992 Diamond and diamond-like films *Thin Solid Films* **216** 126–33
- [17] Savvides N and Bell T J 1992 Microhardness and Young's modulus of diamond and diamondlike carbon films *J. Appl. Phys.* **72** 2791–6